Published in final edited form as:
Biomaterials. 2010 August ; 31(23): 6004–6012. doi:10.1016/j.biomaterials.2010.04.013.

Bone Regeneration Mediated by Biomimetic Mineralization of a Nanofiber Matrix

Alvaro Mata[1,^], **Yanbiao Geng**[1], **Karl Henrikson**[2], **Conrado Aparicio**[1], **Stuart Stock**[3], **Robert L. Satcher**[4,5], and **Samuel I. Stupp**[1,4,6,7,*]

[1]Institute for BioNanotechnology in Medicine Northwestern University, Chicago, IL 60611

[2]Department of Biomedical Engineering Northwestern University, Chicago, IL 60208

[3]Department of Molecular Pharmacology and Biological Chemistry Northwestern University, Chicago, IL 60611

[4]Feinberg School of Medicine Northwestern University, Chicago, IL 60611

[5]Department of Orthopaedic Oncology The University of Texas MD Anderson Cancer Center, Houston, TX 77030

[6]Department of Materials Science and Engineering Northwestern University, Chicago, IL 60208

[7]Department of Chemistry Northwestern University, Chicago, IL 60208

Abstract

Rapid bone regeneration within a three-dimensional defect without the use of bone grafts, exogenous growth factors, or cells remains a major challenge. We report here on the use of self-assembling peptide nanostructured gels to promote bone regeneration that have the capacity to mineralize in biomimetic fashion. The main molecular design was the use of phosphoserine residues in the sequence of a peptide amphiphile known to nucleate hydroxyapatite crystals on the surfaces of nanofibers. We tested the system in a rat femoral critical size defect by placing pre-assembled nanofiber gels in a 5 mm gap and analyzed bone formation with micro-computed tomography and histology. We found within 4 weeks significantly higher bone formation relative to controls lacking phosphorylated residues and comparable bone formation to that observed in animals treated with a clinically used allogenic bone matrix.

1. Introduction

Bone grafts are being used increasingly to stimulate healing of skeletal fractures that have failed to heal, to promote healing between two bones across a diseased joint, and also to replace and regenerate bone lost due to trauma, infection, or disease [1-3]. Worldwide, 2.2 million bone graft procedures are performed annually, which represent about 10% of all orthopedic operations [4,5] Of these, the current standard bone graft material is autogenous cancellous bone, which provides osteoconductive and osteoinductive stimuli and, in the US

*Corresponding author: Northwestern University Chicago, IL 60611 Tel: (312) 503-6713 Fax: (312) 503-2482 s-stupp@northwestern.edu .
^Current address for Alvaro Mata is Nanotechnology Platform, Parc Cientific Barcelona, Barcelona, Spain 08028

alone, accounts for more than 50% of the 500,000 annual bone graft procedures [6,7]. This bone grafting strategy can lead to complications such as pain, infection, scarring, blood loss, and donor-site morbidity [7]. At the same time allogenic demineralized bone matrix, the primary alternative in skeletal reconstructive surgery, lacks the osteoactive capacity of autografts and carries the risk of introducing infectious agents or immune rejection [2]. Finding effective bone regeneration strategies that avoid the need for autografts or allografts is therefore an important objective in the context of an aging population [1].

An extensive research effort has been dedicated to the search of an optimum bone bioactive scaffold [1,2,8]. Some previous work has focused on improving the efficacy of autografts and allografts, for example by incorporating bone marrow aspirates or platelet-rich plasma to increase the population of bone progenitor cells [9,10] as well as the concentration of growth factors to stimulate cells [11-13]. Other research has been directed towards enhancing the bioactivity of synthetic and natural materials for bone regeneration. Some examples include developing hybrid biopolymers of poly(ethylene glycol)-fibrinogen [14], modified calcium phosphate materials [15,16] composites [17], synthetic materials for bone morphogenic protein delivery [18,19], and rapid prototyping fabrication techniques with [20] or without [21] genetically engineered cells.

Our laboratory has developed molecularly designed peptide amphiphile (PA) materials capable of self-assembling into well-defined nanofibers [22,23] that display specific bioactive epitopes on their surface to control cell behavior both *in vitro* [24-26] and *in vivo* [27,28]. Nanofiber-forming PA molecules contain a peptide segment with one domain that has a strong propensity to form extended β-sheets and a second domain with amino acid residues important to bioactivity. The β-sheet domain promotes the assembly of molecules into fibrous aggregates and discourages aggregation into spherical nanostructures [29,30]. The second segment, covalently grafted to the peptide, has greater hydrophobicity than any peptide and forms the core of fibers upon self-assembly, thus ensuring display of the peptide segments at an aqueous interface. The resulting self-assembled PA nanofibers are a few nanometers in diameter and can easily attain lengths of microns. The architecture of these systems is therefore highly biomimetic of the fibrous elements commonly found in extracellular matrix (ECM) such as collagen fibrils. Furthermore, several bioactive cues can be presented simultaneously by co-assembling multiple PA molecules bearing different signals [31].

In this work we have investigated the impact of a matrix with biomimetic elements on bone regeneration within a defect. In addition to a collagen-like fibrilar architecture (cylindrical nanofibers), the biomimetic features of the matrix include its ability to nucleate *in vivo* hydroxyapatite crystals that resemble those in natural bone. Previous work form our laboratory demonstrated first in two-dimensional experiments the ability of peptide amphiphile nanofibers with phosphoserine residues near their surfaces to nucleate thin hydroxyapatite crystals with their c-axis parallel to nanofibers [22]. This crystallographic relationship is observed in biology with respect to the long axis of collagen fibrils. Very recently, we extended this work to three-dimensional networks of similar nanofibers by promoting mineralization in well established osteogenic media containing organophosphates and the enzyme alkaline phosphatase [32]. We test here *in vivo* these three dimensional biomimetic systems as a matrix to promote bone regeneration using an orthotopic rat femoral critical-size defect model. Using co-assembly of two PA molecules, we also tested the combined effect on bone bioactivity of the fibronectin epitope RGDS and the phosphoserine residues for hydroxyapatite nucleation.

2. Materials and methods

Peptide amphiphile synthesis and characterization

PA molecules were synthesized using methods previously described [31]. Solid-phase peptide synthesis (SPPS) was performed using Wang resin (EMD) with standard 9-fluorenylmethoxycabonyl (Fmoc) protected amino acids (EMD Biosciences, San Diego, CA) in *N,N*-dimethylformamide (DMF), diisopropylethylamine (DIEA) and 2-(1H-benzotriazol-1-yl)-1,1,3,3-tetramethyluronium hexafluorophosphate (HBTU). Each PA was synthesized using orthogonal protecting group chemistry using a CSBio peptide synthesizer CS136 (Menlo Park, CA), and palmitic acid was coupled directly to the N terminus of the peptide sequence to create a hydrophobic tail. After synthesis, the PA was cleaved from the resin using TFA/triisopropylsilane (TIS)/water (95:2.5:2.5), precipitated with ice-cold ether, solubilized in water, and dried by lyophilization. The product was then purified using a Varian ProStar Model 210 preparative-scale reverse-phase HPLC on a Waters Atlantis column, and characterized using a PE Biosystems Voyager-DE PRO MALDI-TOF mass spectrometer and a Hewlett-Packard 1050 RP-HPLC. Samples were then lyophilized and stored at −20° C until use.

PA matrix preparation

The PA molecules used to formulate the various matrices were first dissolved separately in deionized (DI) water to a concentration of 20 mM. These PA solutions were either gelled and implanted separately [S(P)-PA and S-PA] or in some cases were mixed, gelled, and implanted as two-PA systems. These two-PA implants included 95% S(P)-PA and 5% RGDS-PA [RGDS+S(P)-PA] as well as 95% Filler-PA and 5% RGDS-PA (RGDS+Filler-PA). These ratios were based on the previous work by Storrie et al in our laboratory, which determined a 95% dilution in a filler PA to be optimum for cellular recognition of the RGDS epitope [25]. The various PA solutions were gelled immediately prior to implantation by combining with a solution of 40 mM $CaCl_2$ (1:1 by vol.) to induce formation of a gel with final PA concentration of 20 mM.

Animal surgeries

An established critical-size rat femoral defect model was used in this study [54]. Surgical and animal care procedures were reviewed and approved by Northwestern University's Animal Care and Use Committee. The study used a total of forty-seven 25-week old male Sprague Dawley rats (Harlan, Indianapolis, IN) with preoperative weights ranging from 350 to 400 g. The animals were anesthetized by intraperitoneal injection of ketamine (100 mg/kg) and xylazine (5 mg/kg), followed by subcutaneous procaine penicillin (60,000 international units) to minimize the risk of infection and buprenex (0.5 mg/kg) for pain management. The animal was placed on its side and the femoral diaphysis was approached through a lateral incision in the skin. Then, the subcutaneous tissues and fascia were incised, the muscle was circumferentially stripped, and the femur exposed. Ti plates (Synthes USA, Paoli, PA) with 1.5 mm diameter holes were cut to a length of ~2.5 cm in length (leaving five holes/plate) and laid on the exposed femur to serve as a template to ensure appropriate positioning of the drill holes. The Ti plate was fixed with four 1.1 mm diameter screws positioned in the proximal and distal diaphysis of the femur, leaving the middle hole to overlay the defect. The plate and screws were removed and a 5 mm long defect was created using a high-speed oscillating saw (Synthes USA, Paoli, PA), followed by repositioning and fixation of the Ti plate (Figure 1D). A 200 μL PA gel or DBM (200 mg) was positioned in the fracture site, filling the gap, and bridging the bone pieces (Figure 1E). The muscle and skin were each repositioned and sutured to close the wound and the animals were left to recover. Pain management consisted of administering buprenex once every 12 h and meloxicam once every 24 h for the first 48 h after implantation. Animals were sacrificed

either at 24 or 48 h for the PA localization experiments or at 4 weeks for the bone regeneration experiments.

Surgical placement of PA matrices

Following the surgical procedure described above, two animals were analyzed to determine the localization of the PA implant within the fracture site after implantation. These animals were implanted with a non-bioactive PA containing a pyrene segment [55], which is fluorescent when excited with 365 nm UV light. Animals were sacrificed at either 24 or 48 h after implantation and their femurs exposed and irradiated with a UV lamp (Spectronics Corporation, Westbury, NY) to qualitatively observe the location of the PA material.

Bone regeneration experiments

Four types of PA implants were tested to assess their bone regeneration potential, and animals were sacrificed 4 weeks after implantation. The femurs were carefully harvested and fixed in 10% formalin prior to microCT analysis to quantify new bone formation and histological evaluation to analyze the biological response. In order to account for random variations between experiments, statistical significance was defined at the level of significance of 0.05 using a Student's t-test performed in JMP Statistical Discovery Software (SAS Institute Inc., Cary, NC).

Micro-computed tomography

Samples were removed from the 10% formalin, air dried for 10 min, and embedded in polydimethylsiloxane (PDMS) (Sylgard 184, Dow Corning, Midland, MI) to immobilize the bone while removing the Ti-plate. A MicroCT 40 system (Scanco Medical, PA, USA) operated at 45 kV and 177 μA was used to collect data for reconstruction of volume encompassing the surgically produced gap in the bone of the rat femur. Each femur was oriented with its axis parallel to the scanner's rotation axis. A total of 500 projections of 512 spatial samples and 0.3 s integration time per projection were recorded and used to produce the $(1024)^2$ reconstructions. The specimen dimensions dictated that reconstructions employed 31 μm isotropic volume elements (voxels), and 280 slices (7.8 mm) were required to span the volume between the fixation holes nearest the bone gap. Inspection of many preliminary specimens differentiated the less heavily mineralized bone formed after the surgery from more heavily mineralized bone at the cut ends of the femur. The amount of bone forming in the gap was quantified using the Scanco software suite in two steps. The combined signal from newly formed bone and cut bone ends was quantified using a threshold $\mu > 1.35\ cm^{-1}$. The femoral diaphysis was identified using threshold $\mu > 3.2\ cm^{-1}$. The difference between the two volumes was the volume of bone forming in the gap. Note that the most heavily mineralized bone in the cortex of the femoral diaphysis had $3.5 < \mu < 4.5\ cm^{-1}$. For comparison, at 45 kV, the X-ray effective energy is about 24 keV, and one expects mature bone to have linear attenuation coefficients up to $\mu \sim 4.5\ cm^{-1}$ for these operating conditions [56].

Histology

Samples for histological analysis were fixed (10% neutral buffered formalin), decalcified (DecalStat, Decal Chemical Corporation), dehydrated in ethanol and xyline, and embedded in paraffin wax for sectioning. Three 4 μm thick sections, separated by 50 μm distances and cut sagittally with respect to the femur, were performed on each sample. Sections were stained with H&E, Masson's trichrome, or Goldner's trichrome to identify cells and tissues characteristic of the bone regeneration process.

Fixation for scanning electron microscopy

Scanning electron microscopy (SEM) was used to visually analyze the nano- and microstructure of the implanted PA gels. Gels were fixed in a solution of 2% in glutaraldehyde/3% sucrose PBS at 4° C. After 1 h, substrates were rinsed twice with PBS for 30 min at 4° C and washed with deionized (DI) water for 5 min. Dehydration was performed by placing the substrates in 50% ethanol (in DI water) for 10 min and replacing it every 10 min while increasing the concentration to 60, 70, 80, 90, 95, and 100% ethanol. The liquid ethanol was removed while preserving the PA topographical patterns using critical point drying.

3. Results

Self-assembly and preparation of PA nanofibrous matrixes

The four PA molecules shown below were synthesized, purified, and their chemical structure verified by MALDI-TOF mass spectrometry and analytical HPLC. One molecule contained a phosphoserine residue (S(P)-PA), a second molecule contained the RGDS epitope (RGDS-PA), and two additional molecules served as controls. One control contained a serine residue without phosphorylation (S-PA) and the second one was a non-bioactive PA molecule (Filler-PA), which was used as a spacer in the nanofiber assemblies to improve the availability of RGDS epitopes [25].

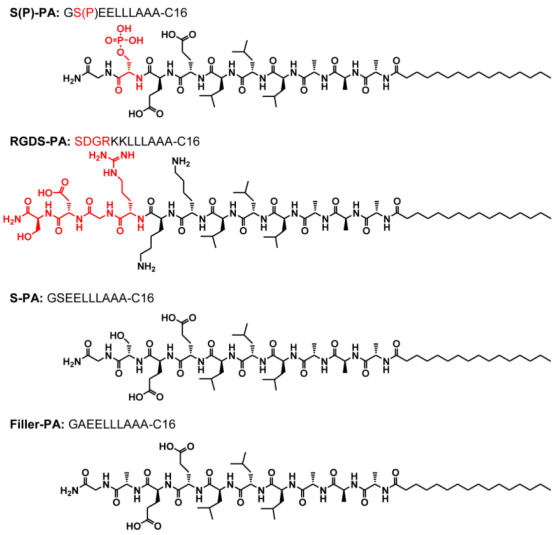

The PA molecules were first dissolved separately in deionized (DI) water to a concentration of 40 mM and gelled immediately prior to implantation by combining with a solution of 40 mM $CaCl_2$ (1:1 by volume) to create a gel with final PA concentration of 20 mM. Scanning electron microscopy of these gels reveals networks of bundled nanofibers with diameters of about 30 nm (see Figure 1B). These materials were used as scaffolds to assess their potential to promote bone regeneration using an orthotopic 5-mm wide critical-sized rat femoral defect model. All nanofiber gels exhibited sufficient strength to be extruded through a 4 mm diameter pipette tip and positioned into the defect (Figure 1C-E). In addition to the PA gel matrices we also implanted in the defects samples of human demineralized bone matrix (DBM) which served as positive controls while defects left untreated served as negative controls (see Table 1).

Localization of PA gels within the fracture site

In order to determine if the PA gels could remain localized in the defect up to 48 h after implantation, we used a PA molecule containing a fluorescent pyrene segment (Pyrene-PA) (Figure 2A). Figure 2 illustrates the positioning of the PA gel during surgery as well as its distribution within the defect region after 24 and 48 h of implantation. Although PA gels were initially positioned to fill the bone defect and surround the cut ends of the femur (Figure 2C), the PA was dispersed locally after both 24 and 48 h. This suggests that although the gel may be displaced from the original location and fragmented due to relative movement of the tissues (during animal locomotion), the PA material remains present within the gap, coating the bone and muscle tissue surrounding the osteotomy site (Figure 2D, E).

Quantification of bone formation by micro-computed tomography

All animals became mobile within 3-4 h after surgery. Significant differences were observed between groups (Table 1) in both the micro computed tomography (microCT) and histological analysis. The microCT quantification demonstrated that the animals receiving the RGDS+S(P)-PA gel revealed the highest mean volume of ossified tissue within the callus of all tested groups (24.80 mm^3). This mean value of ossified tissue was significantly greater ($p<0.05$) than that observed in untreated animals (10.21 mm^3) as well as those treated with S-PA (14.16 mm^3) and RGDS+Filler-PA (13.45 mm^3) (Figure 3,4). Interestingly, the amount of ossified tissue in animals treated with RGDS+S(P)-PA was statistically indistinguishable from that observed in animals treated with S(P)-PA alone (18.95 mm^3). Also, this value was significantly greater ($p<0.05$) than that in untreated animals (10.21 mm^3) (Figure 3,4). Furthermore, animals treated with S(P)-containing PA nanofibers exhibited similar bone regeneration than those treated with allogenic matrix (DBM) (23.61 mm^3). Other groups have demonstrated the absence of an immune reaction by implanting non-athymic animals with human DBM [33,34], and therefore we interpret the observed similarity in bone regeneration as an attribute of the synthetic bioactive nanofibers capable of promoting biomimetic mineralization. In general, although newly formed ossified tissue was evident in all samples within the gap region and on the proximal and distal cut ends of the femoral diaphysis, the amount was clearly different and dependent on the treatment group (Figure 4, 5).

Histological analysis of bone formation

Histological sections also revealed greater bone formation on animals treated with the RGDS+S(P)-PA gel matrix compared to untreated and relative to those treated with the serine and RGDS systems. Interestingly, the phosphorylated serine matrix led to similar bone formation as RGDS+S(P)-PA and DBM (Figure 5A-C). In accordance with natural bone fracture healing, signatures of both endochondral and intramembranous ossification were observed [6]. Endochondral ossification was present primarily within the original femoral defect site, extending axially from the cut surfaces of the pre-existing cortical bone into the inner surface of the callus (Figure 5D). Here, periosteal tissue was observed surrounding cartilaginous tissue rich in chondrocytes, immediately followed by woven ossified tissue embedded with osteoblastic cells (Figure 5E). Moreover, animals treated with RGDS+S(P)-PA gel matrices also exhibited intramembranous ossification (areas of ossified woven bone tissue with no cartilage), primarily on the inside and outside surfaces of the original cortex of the femoral diaphysis. The presence of woven ossified tissue within the callus was also established through observation of birefringence. Viewing under polarized light between cross-polars, newly formed woven bone is characterized by small birefringent domains [35], whereas lamellar bone is characterized by larger birefringent ones. In our experiments, large birefringent domains were observed along the original bone cortex while small birefringent ones were present within the callus (data not shown). Finally, daily observation of the animals and histological analysis revealed no evidence of any immune

reaction. Furthermore, histological sections revealed neither inflammation nor presence of any cells that would be expected to be present in the case of an immune reaction such as lymphocytes, neutrophils, or osteoclasts.

4. Discussion

The objective of the present study was to determine the *in vivo* osteogenic potential of self-assembling PAs comprising bioactive epitopes specifically designed to promote bone regeneration. The main design feature of our PA material was the incorporation of S(P) segments within well-defined self-assembled nanofibers with ECM-like fibrous architectures. The objective of this approach was to generate a completely artificial bone-bioactive matrix that mimics elements of bone biomineralization [36]. The ability of this matrix to emulate partly these processes in a three dimensional fibrous matrix has been described by two previous publications from our laboratory [22,32]. The artificial matrix used here might be considered a mimic of bone sialoprotein, which is rich in phosphorylated serine residues, has a high affinity for calcium ions, and is known to play a key role in bone mineralization [8,37]. Therefore, the central molecular feature of our strategy was to design PAs that could generate three dimensional fibrous matrices that display high concentrations of phosphorylated serine residues on their surfaces. These nanofibers would not only introduce *in vivo* biomimetic nucleation of hydroxyapatite and its biological consequences, but would also help augment the overall deposition of mineral within the defect. In order to further enhance bioactivity of the artificial matrix, we took advantage of co-assembly of two molecules in these supramolecular systems and combined S(P)-PA molecules with RGDS-PA molecules. PA molecules with the RGDS fibronectin epitope were introduced to promote integrin-mediated adhesion of cells that participate in bone regeneration such as mesenchymal stem cells, osteoprogenitor cells, osteoblasts, and vascular tissue cells [38-40].

The RGDS+S(P)-PA gel matrices led to the highest average amount of ossified tissue within the callus and at a level that was statistically equivalent to those treated with artificial matrices only containing the phosphorylated serine residues [S(P) PA] or the type of allogeneic demineralized bone matrix used clinically at the present time (Figures 3, 4). This result highlights the importance of biomimetic mineralization of therapeutic matrices to bone bioactivity. We know from previous work that showed phosphorylated serine PA nanofibers nucleate biomimetic crystals of hydroxyapatite (crystallographically aligned with the fiber axis as it occurs with respect to collagen in biology) in both two dimensional [22] and three dimensional matrices under physiological conditions [32]. RGDS-containing PAs were shown previously by our group to promote cell adhesion in vitro [25,41-43]. In this study there was no significant difference between animals treated with RGDS+Filler-PA and untreated ones, but we cannot rule out that some synergy occurred between both PAs (from 18.95 mm^3 with S(P)-PA to 24.80 mm^3 with RGDS+S(P)-PA), and optimization of this effect might be possible in future studies. Furthermore, qualitative observations of the different PA gels revealed a similar mechanical stability among all the different groups. Therefore, it is possible that the S(P)-containing nanofibers are presenting a favorable hydroxyapatite nucleation environment within and around the fracture site, which is promoting earlier biomineralization compared to those of other treatments and controls and leading to a higher content of ossified tissue within the callus after 4 weeks.

Bone regeneration in response to serine PAs was not statistically different from that found in untreated defects whereas regeneration was enhanced in response to phosphorylated serine PAs. There are several physical and biological mechanisms through which the bioactive PA nanofiber matrix may be enhancing bone formation. First the PA gel tends to coat the surface of the bone, both over the periosteum and on the cross-section where the defect was created, including close to the medullary canal (Figure 2F). This flow of the PA matrix may

promote its contact with osteoprogenitor and mesenchymal stem cells (present in the periosteum and bone marrow) and facilitate their migration towards the defect site. In addition to assisting this cell colonization toward bone repair, it is possible that the biomimetic HA crystals on S(P)-PA nanofibers may be stimulating cellular events. Non-collagenous proteins such as phosphophoryn or bone sialoprotein, which are rich in S(P) residues, not only play a role in nucleation of mineral but have been shown to stimulate gene expression and enhance osteoblast differentiation of MSCs *in vitro* [44]. Furthermore, other groups have recently described an Osteoconductive [45] and Osteoinductive [46-48] effect of calcium phosphate minerals on mesenchymal stem cells. Thus an earlier presence of this mineralized matrix as a result of the highly concentrated S(P) residues on the surface of the nanofibers could stimulate local mesenchymal stem cell population into an osteoblastic phenotype. Furthermore, this HA-containing niche may also be stimulating osteoclast activity [49], which would subsequently stimulate osteoblasts to begin the formation of new bone [50].

On the chemical side the phosphorylated matrix is a natural attractant for both calcium and phosphate ions that could be harvested by enzymes such as alkaline phosphatase (ALP), known to play an early role in bone regeneration [51]. PA nanofibers self-assemble through charge neutralization by incorporation of calcium chloride and therefore have a high calcium affinity, a critical factor for biomineralization [52,53]. At the same time, under physiological conditions and in the presence of ALP, phosphorylated PAs have been shown to nucleate biomimetic HA crystals with their c-axes aligned along the axis of the nanofibers within a few days [32]. We hypothesize that this process takes place *in vivo* since phosphate ions can be harvested from the artificial phosphate-rich S(P)-PA matrix by ALP [51]. Furthermore, an enhanced osteoblastic activity may be promoting expression of ALP thus offering further synergy in bone repair relative to animals without treatment. In this context, S(P)-containing artificial matrices may be emulating the positive effects of DBM on bone repair which is known to contain acidic proteins and preserved collagen structures important in HA mineralization [5].

5. Conclusion

Artificial and biomimetic matrices for bone regeneration have been evaluated in a non-healing rat femoral defect. Enhanced bone regeneration has been linked to the presence of phosphorylated serine residues on the supramolecular nanofibers of these matrices which promote formation of biomimetic bone crystals. These bioactive matrices could address the clinical problems of autologous bone grafts or allografts from banked human bone.

Acknowledgments

Funding for this study was provided by the National Institutes of Health/National Institute of Dental & Craniofacial Research (NIH/NIDCR), Grant No. 5R01DE015920-3. This work made use of Central Facilities supported by the MRSEC program of the National Science Foundation (DMR-0520513) at the Materials Research Center of Northwestern University. Electron microscopy was performed in the Electron Probe Instrumentation Center (EPIC) facility of the NUANCE Center at Northwestern University, and is supported by NSF-NSEC, NSF-MRSEC, Keck Foundation, the State of Illinois, and Northwestern University. MALDI and ESI analysis were performed at the IMSERC Center and confocal microscopy performed at the Cell Imaging Facility both at Northwestern University. We thank Mr. Ben Myers, Dr. William Russin, Mr. Lennel Reynolds, and Dr. Teng-Leong Chew for assistance with the various microscopy techniques. We also would like to thank Dr. William Laskin, Dr. Erik Spoerke, Shawn Anthony, Dr. Tomiko Fukuda, Dr. Liam Palmer, and Dr. Ramille Capito for important discussions. Conrado Aparicio would like to thank the Generalitat de Catalunya and the Technical University of Catalunya, Barcelona, Spain for fellowship support.

References

1. Stevens MM. Biomaterials for bone tissue engineering. Materials Today 2008;11(5):18–25.

2. Dawson JI, Oreffo ROC. Bridging the regeneration gap: stem cells, biomaterials and clinical translation in bone tissue engineering. Arch Biochem Biophys 2008;473:124–32. [PubMed: 18396145]
3. Bauer TW, Muschler GF. Bone graft materials. An overview of the basic science. Clin Orthop Relat Res 2000;371:10–27. [PubMed: 10693546]
4. Lohmann H, Grass G, Rangger C, Mathiak G. Economic impact of cancellous bone grafting in trauma surgery. Arch Orthop Trauma Surg 2007;127:345–48. [PubMed: 17294203]
5. Planell, JA.; Lacroix, D.; Best, S.; Merolli, A. Bone Repair Biomaterials. Woodhead Publishing; Cambridge: 2009.
6. Fleming JE, Cornell CN, Muschler GE. Bone cells and matrices in orthopedic tissue engineering. Orthop Clin. North Am 2000;31(3):357–67. [PubMed: 10882463]
7. Palmer LC, Newcomb CJ, Kaltz SR, Spoerke ED, Stupp SI. Biomimetic systems for hydroxyapatite mineralization inspired by bone and enamel. Chem Rev 2008;108:4754–83. [PubMed: 19006400]
8. Sen MK, Miclau T. Autologous iliac crest bone graft: should it still be the gold standard for treating nonunions? Injury 2007;38(Suppl 1):S75–80. [PubMed: 17383488]
9. Smiler D, Soltan M, Lee JW. A histomorphogenic analysis of bone grafts augmented with adult stem cells. Implant Dent 2007;16(1):42–53. [PubMed: 17356371]
10. Helms JA, Amasha RR, Leucht P. Bone voyage: An expedition into the molecular and cellular parameters affecting bone graft fate. Bone 2007;41(4):479–85. [PubMed: 17692586]
11. Hisamitsu J, Yamazaki M, Suzuki H, Hashimoto M, Nakajima A, Moriya H. Gene expression for type-specific collagens in osteogenic protein-1 (rhBMP-7)-induced lumbar intertransverse process fusion in rabbits. Connect Tissue Res 2006;47(5):256–63. [PubMed: 17118747]
12. Ito H, Koefoed M, Tiyapatanaputi P, Gromov K, Goater JJ, Carmouche J, et al. Remodeling of cortical bone allografts mediated by adherent rAAV-RANKL and VEGF gene therapy. Nat Med 2005;11(3):291–97. [PubMed: 15711561]
13. Peled E, Boss J, Bejar J, Zinman C, Seliktar D. A novel poly(ethylene glycol)-fibrinogen hydrogel for tibial segmental defect repair in a rat model. J Biomed Mater Res A 2007;80A(4):874–84. [PubMed: 17072852]
14. Walsh WR, Vizesi F, Michael D, Auld J, Langdown A, Oliver R, et al. β-TCP bone graft substitutes in a bilateral rabbit tibial defect model. Biomaterials 2008;29(3):266–71. [PubMed: 18029011]
15. Kroese-Deutman HC, Wolke JGC, Spauwen PHM, Jansen JA. Closing capacity of cranial bone defects using porous calcium phosphate cement implants in a rabbit animal model. J Biomed Mater Res A 2006;79A(3):503–11. [PubMed: 16788974]
16. Kamakura S, Sasaki K, Honda Y, Anada T, Suzuki O. Octacalcium phosphate combined with collagen orthotopically enhances bone regeneration. J Biomed Mater Res Part B Appl Biomater 2006;79B(2):210–17. [PubMed: 16615073]
17. Chu TMG, Warden SJ, Turner CH, Stewart RL. Segmental bone regeneration using a load-bearing biodegradable carrier of bone morphogenetic protein-2. Biomaterials 2007;28(3):459–67. [PubMed: 16996588]
18. Oest ME, Dupont KM, Kong HJ, Mooney DJ, Guldberg RE. Quantitative assessment of scaffold and growth factor-mediated repair of critically sized bone defects. J Orthop Res 2007;25(7):941–50. [PubMed: 17415756]
19. Byers BA, Guldberg RE, Hutmacher DW, García AJ. Effects of Runx2 genetic engineering and in vitro maturation of tissue-engineered constructs on the repair of critical size bone defects. J Biomed Mater Res A 2006;76A(3):646–55. [PubMed: 16287095]
20. Rohner D, Hutmacher DW, Cheng TK, Oberholzer M, Hammer B. In vivo efficacy of bone-marrow-coated polycaprolactone scaffolds for the reconstruction of orbital defects in the pig. J Biomed Mater Res 2003;66B:574–80.
21. Hartgerink JD, Beniash E, Stupp SI. Self-assembly and mineralization of peptide-amphiphile nanofibers. Science 2001;294(5547):1684–88. [PubMed: 11721046]
22. Hartgerink JD, Beniash E, Stupp SI. Peptide-amphiphile nanofibers: A versatile scaffold for the preparation of self-assembling materials. Proc Natl Acad Sci USA 2002;99(8):5133–38. [PubMed: 11929981]

23. Silva GA, Czeisler C, Niece KL, Beniash E, Harrington DA, Kessler JA, et al. Selective differentiation of neural progenitor cells by high-epitope density nanofibers. Science 2004;303(5662):1352–55. [PubMed: 14739465]
24. Storrie H, Guler MO, Abu-Amara SN, Volberg T, Rao M, Geiger B, et al. Supramolecular crafting of cell adhesion. Biomaterials 2007;28(31):4608–18. [PubMed: 17662383]
25. Beniash E, Hartgerink JD, Storrie H, Stendahl JC, Stupp SI. Self-assembling peptide amphiphile nanofiber matrices for cell entrapment. Acta Biomater 2005;1(4):387–97. [PubMed: 16701820]
26. Rajangam K, Behanna HA, Hui MJ, Han X, Hulvat JF, Lomasney JW, et al. Heparin Binding Nanostructures to Promote Growth of Blood Vessels. Nano Lett 2006;6:2086–90. [PubMed: 16968030]
27. Huang Z, Sargeant TD, Hulvat JF, Mata A, Bringas P Jr, Koh CY, et al. Bioactive Nanofibers Instruct Cells to Proliferate and Differentiate During Enamel Regeneration. J Bone Miner Res Dec;2008 23(12):1995–2006. [PubMed: 18665793]
28. Jiang H, Guler MO, Stupp SI. The internal structure of self-assembled peptide amphiphiles nanofibers. Soft Matter 2007;3:454–62.
29. Velichko YS, Stupp SI, de la Cruz M Olvera. Molecular simulation study of peptide amphiphile self-assembly. J Phys Chem 2008;B112:2326–34.
30. Sargeant TD, Guler MO, Oppenheimer SM, Mata A, Satcher RL, Dunand DC, et al. Hybrid bone implants: Self-assembly of peptide amphiphile nanofibers within porous titanium. Biomaterials 2008;29(2):161–71. [PubMed: 17936353]
31. Spoerke ED, Anthony SG, Stupp SI. Enzyme directed templating of artificial bone mineral. Adv Mater 2009;21(4):425–30.
32. Cho KS, Choi SH, Han KH, Chai JK, Wikesjö UM, Kim CK. Alveolar bone formation at dental implant dehiscence defects following guided bone regeneration and xenogeneic freeze-dried demineralized bone matrix. Clin Oral Implants Res 1998;9(6):419–28. [PubMed: 11429943]
33. Jung UW, Moon HI, Kim CS, Lee YK, Kim CK, Choi SH. Evaluation of different grafting materials in three-wall intra-bony defects around dental implants in beagle dogs. Current Applied Physics 2005;5(5):507–11.
34. Bromage TG, Goldman HM, Mcfarlin SC, Warshaw J, Boyde A, Riggs CM. Circularly polarized light standards for investigations of collagen fiber orientation in bone. Anat Rec B New Anat 2003;274(1):157–68. [PubMed: 12964206]
35. Mackie EJ. Osteoblasts: novel roles in orchestration of skeletal architecture. Int J Biochem Cell Biol 2003;35:1301–05. [PubMed: 12798343]
36. Ganss B, Kim RH, Sodek J. Bone sialoprotein. Crit Rev Oral Biol Med 1999;10(1):79–98. [PubMed: 10759428]
37. Sawyer AA, Hennessy KM, Bellis SL. The effect of adsorbed serum proteins, RGD and proteoglycan-binding peptides on the adhesion of mesenchymal stem cells to hydroxyapatite. Biomaterials 2007;28(3):383–92. [PubMed: 16952395]
38. Behravesh E, Zygourakis K, Mikos AG. Adhesion and migration of marrow-derived osteoblasts on injectable in situ crosslinkable poly(propylene fumarate-co-ethylene glycol)-based hydrogels with a covalently linked RGDS peptide. J Biomed Mater Res 2003;A65(2):260–70.
39. Hersel U, Dahmen C, Kessler H. RGD modified polymers: biomaterials for stimulated cell adhesion and beyond. Biomaterials 2003;24:4385–415. [PubMed: 12922151]
40. Harrington DA, Cheng EY, Guler MO, Lee LK, Donovan JL, Claussen RC, et al. Branched peptide-amphiphile as self-assembling coatings for tissue engineering scaffolds. J Biomed Mater Res A 2006;78A:157–67. [PubMed: 16619254]
41. Webber MJ, Tongers J, Renault M, Roncalli JG, Losordo DW, Stupp SI. Development of bioactive peptide amphiphiles for therapeutic cell delivery. Acta Biomater 2009;6:3–11. [PubMed: 19635599]
42. Mata A, Hsu L, Capito R, Aparicio C, Henrikson K, Stupp SI. Micropatterning of bioactive self-assembling gels. Soft Matter 2009;5(6):1228–36. [PubMed: 20047022]
43. Jadlowiec J, Koch H, Zhang X, Campbell PG, Seyedain M, Sfeir C. Phosphophoryn regulates the gene expression and differentiation of NIH3T3, MC3T3-E1, and human mesenchymal stem cells

via the integrin/MAPK signaling pathway. J Biol Chem 2004;279(51):53323–30. [PubMed: 15371433]

44. Murphy WL, Hsiong S, Richardosn TP, Simmons CA, Mooney DJ. Effects of a bone-like mineral film on phenotype of adult human mesenchymal stem cells in vitro. Biomaterials 2005;26:303–10. [PubMed: 15262472]
45. Müller P, Bulnheim U, Diener A, Lüthen F, Teller M, Klinkenberg ED, et al. Calcium phosphate surface promote osteogenic differentiation of mesenchymal stem cells. J Cell Mol Med 2008;12(1):281–91. [PubMed: 18366455]
46. Osathanon T, Linnes ML, Rajachar RM, Ratner BD, Somerman MJ, Giachelli CM. Microporous nanofibrous fibrin-based scaffolds for bone tissue engineering. Biomaterials 2008;29:4091–99. [PubMed: 18640716]
47. Kim SE, Choi HW, Lee HJ, Chang JH, Choi J, Kim KJ, et al. Designing a highly bioactive 3D bone-regenerative scaffold by surface immobilization of nano-hydroxyapatite. J Mater Chem 2008;18:4994–5001.
48. Narducci P, Nicolin V. Differentiation of activated monocytes into osteoclast-like cells on a hydroxyapatite substrate: an in vitro study. Ann Anat 2009;191:349–55. [PubMed: 19447592]
49. Boyle WJ, Simonet WS, Lacey DL. Osteoclast differentiation and activation. Nature 2003;423:337–42. [PubMed: 12748652]
50. Majors AK, Boehm CA, Nitto H, Midura RJ, Muschler GF. Characterization of human marrow stromal cells with respect to osteoblastic differentiation. J Orthop Res 1997;15:546–57. [PubMed: 9379264]
51. He G, Ramachandran A, Dahl T, George S, Schultz D, Cookson D, et al. Phosphorylation of phosphophoryn is crucial for its function as a mediator of biomineralization. J Biol Chem 2005;280:33109–14. [PubMed: 16046405]
52. George A, Bannon L, Sabsay B, Dillon JW, Malone J, Veis A, et al. The Carboxyl-terminal domain on phosphophoryn contains unique extended triplet amino acid repeat sequences forming ordered carboxyl-phosphate interaction ridges that may be essential in the biomineralization process. J Biol Chem 1996;271:32869–73. [PubMed: 8955126]
53. Giannoudis PV, Dinopoulos H, Tsiridis E. Bone substitutes: An update. Injury 2005;36:S20–7. [PubMed: 16188545]
54. Vögelin E, Jones NF, Brekke JH, Lieberman JR. Healing of a critical-sized defect in the rat femus with use of a vascularized periosteal flap, a biodegradable matrix, and bone morphogenic protein. J Bone Joint Surg 2005;87:1323–31. [PubMed: 15930543]
55. Guler MO, Claussen RC, Stupp SI. Encapsulation of pyrene within self-assembled peptide amphiphile nanofibers. J Mater Chem 2005;15:4507–12.
56. Stock SR, Ignatiev KI, Foster SA, Forman LA, Stern PH. MicroCT quantification of in vitro bone resorption of neonatal murine calvaria exposed to TL-1 or PTH. J Struct Biol 2004;147(2):185–99. [PubMed: 15193647]

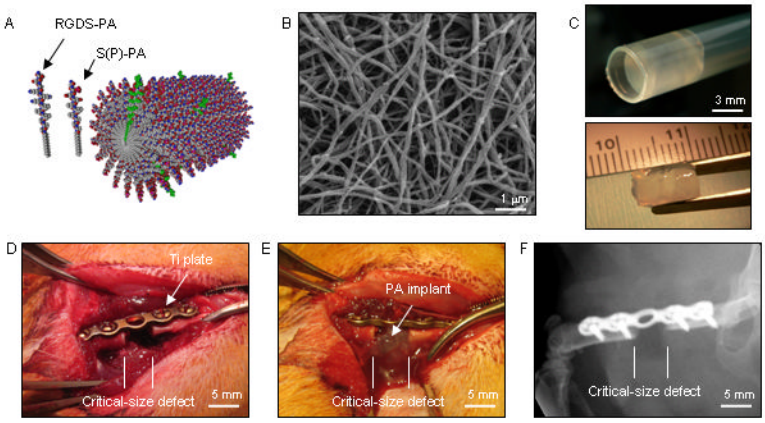

Figure 1.

Setup of experimental PA materials and animal model. (A) Molecular graphics representation of a self-assembled nanofiber formed by co-assembly of the phosphorylated serine peptide amphiphile and the RGDS peptide amphiphile (shown in green). (B) Scanning electron micrograph of a network of RGDS+S(P)-PA nanofibers. (C) 200 μL of 10 mM PA gel implant measuring 4 mm in diameter and 7 mm long prior to implantation. (D) Photograph of the 5 mm long critical size-defect used for the animal model, stabilized with a titanium (Ti) internal plate. (E) Photograph of the site after placement of the PA gel within the defect. (F) Radiograph of a stabilized defect in an animal 24 h after implantation of the PA gel.

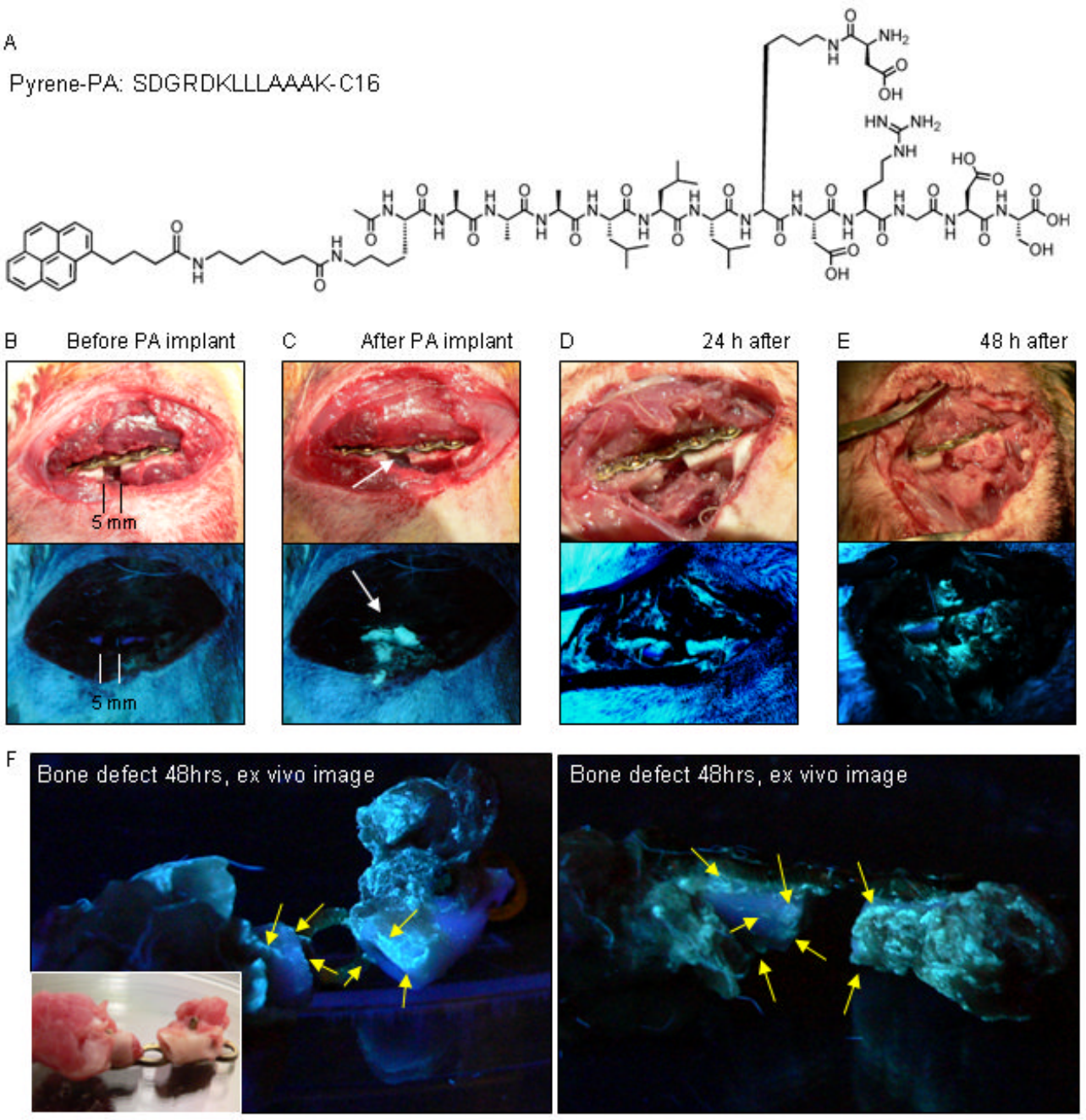

Figure 2.

Presence of PA gel within the defect, before, during, and after surgery. (A) Chemical structure of the fluorescent pyrene-containing molecule used to determine PA gel positioning within the defect. Photographs depict (B) a 5 mm wide critical size defect prior and (C) immediately after fluorescent PA gel implantation (white arrow pointing at location of fluorescent PA). At both 24 h (D) and 48 h (E) after implantation, fluorescent PA gel material was observed to be dispersed but still within and around the fracture site while coating local muscle tissue and (F) the outer and inner surface of the bone.

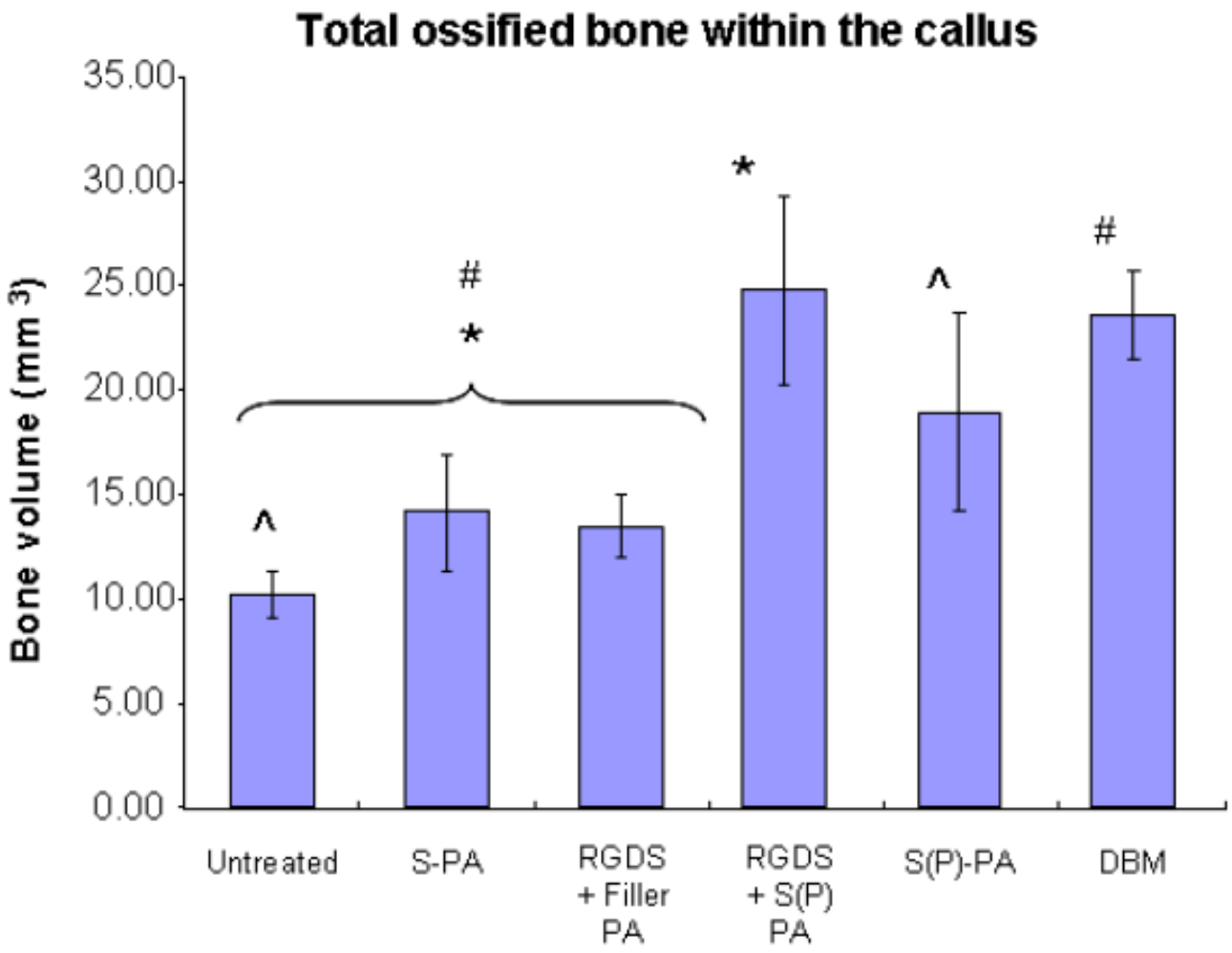

Figure 3.

Quantification of the *in vivo* bone regeneration efficacy of S(P)-containing PAs. Micro-computed tomography quantification of bone regeneration. Total volume of bone tissue within the callus quantified by micro-computed tomography (microCT) scans at 4 weeks postoperative. Animals treated with the S(P)-containing PAs exhibited statistically higher volumes of bone relative to the untreated group. Furthermore, animals treated with RGDS +S(P)-PA also exhibited significantly higher bone volume than those treated with S-PA or RGDS+Filler-PA. Animals treated with RGDS+S(P)-PA artificial matrices also exhibited similar values of regenerated bone as those treated with the positive control DBM (error bars refer to standard error of the mean).

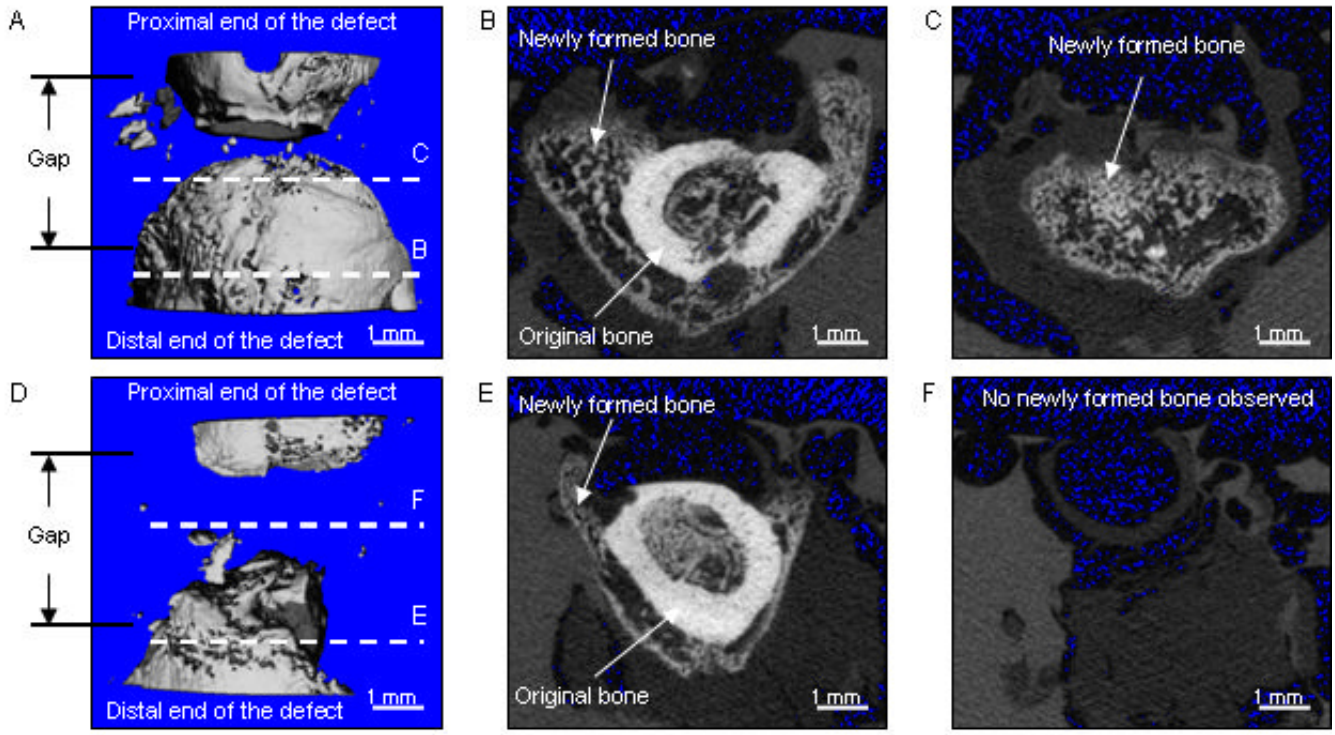

Figure 4.

MicroCT imaging of newly formed bone. Representative microCT images depicting the difference in bone formation observed in animals implanted with RGDS+S(P)-PA within the defect (A-C) versus those left untreated (D-F). Dashed white lines highlight the position of the slices from the RGDS+S(P)-PA treated (B-C) and from the untreated (E-F) animals. Higher levels of new calcified tissue (less dense, gray) was observed in animals treated with the S(P)-containing PA matrix. In these animals new bone formation was observed growing from both ends of the defect tending to bridge the gap (A-C) and expanding radially outwards (B). New bone at the edge of the defect coated both the outside (outer bone surface) and inside (medullary canal) of the original bone (more dense, white), which corresponds to the locations where the PA matrix was observed to coat and be present within 24 and 48 h after implantation (Figure 3).

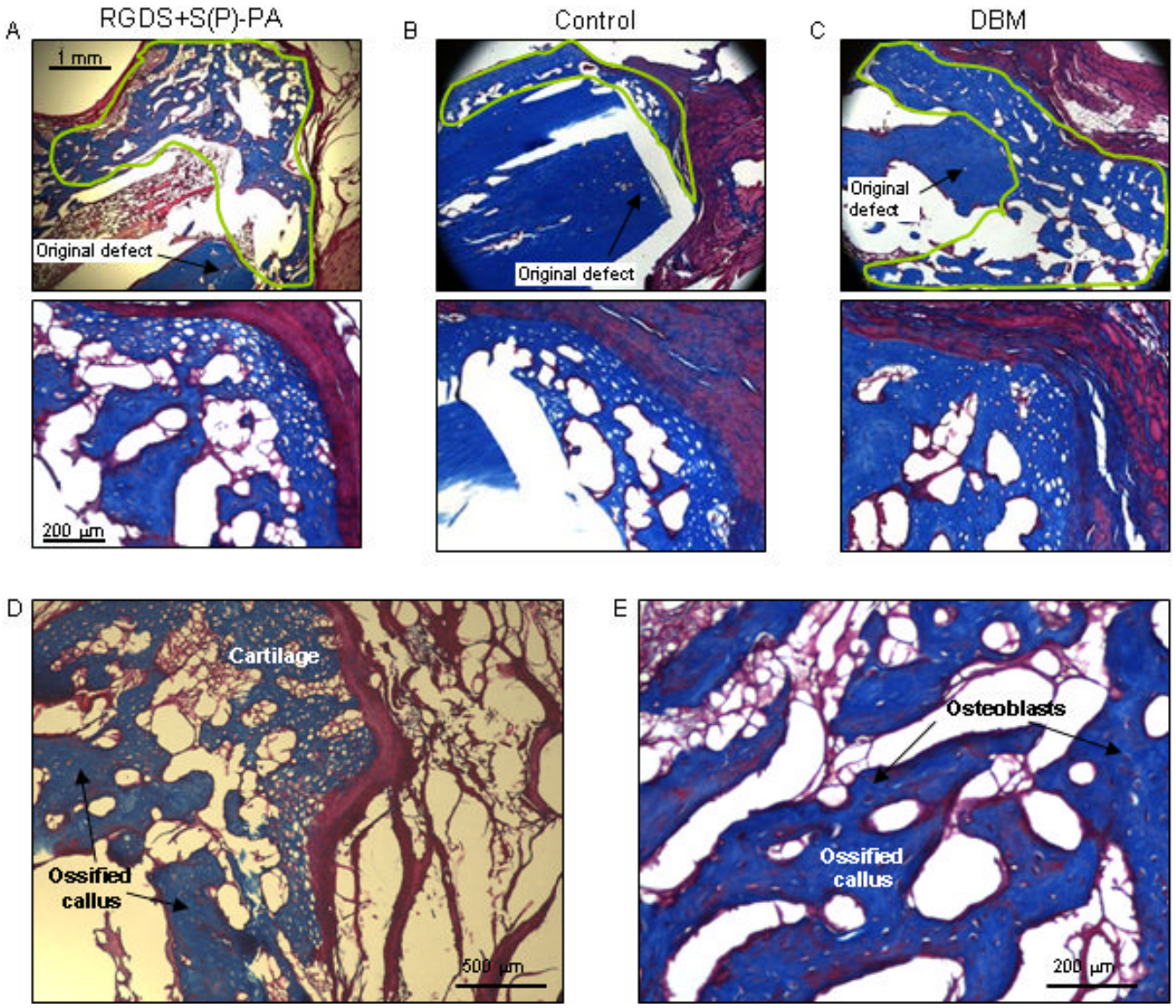

Figure 5.

Histological analysis of newly formed bone. (A-C) Photomicrographs at low (top panel) and high magnification (low panel) of histological sections from the defect site stained with Masson's trichrome. (A) sections from sites treated with RGDS+S(P)-PA, (B) untreated, and (C) treated with DBM (areas within the green outline correspond to ossified tissue within the callus). (D) Sections from defects treated with RGDS+S(P)-PA exhibited primarily signatures of endochondral ossification with a leading periosteum followed by cartilage (embedded with hypertrophic chondrocytes) and ossified tissue. Ossified tissue within the callus (blue) reveals the presence of osteoblasts embedded within it (E).

Table 1

List of peptide amphiphiles tested *in vivo* and their respective number of animals and objective of the experiment

Group	Number of animals	Treatment	Objective of the experiment
1	6	Phosphorylated serine **[S(P)-PA]**	Evaluate effect of mineraliztion epitope alone
2	7	Phosphorylated serine combined with RGDS **[RGDS+S(P)-PA]**	Evaluate combined effect of cell adhesive and mineralization epitopes
3	6	Filler combined with RGDS **(RGDS+Filler-PA)**	Evaluate effect of cell adhesive epitope alone
4	7	Serine **(S-PA)**	Evaluate effect of non-phosphorylated serine
5	6	Demineralized bone matrix **(DBM)**	Evaluate effect of DBM, used as positive control
6	6	Empty defect **(Untreated)**	Evaluate healing in empty defect